remote sensing

MDPI

Article

Using Hyperspectral Remote Sensing to Monitor Water Quality in Drinking Water Reservoirs

Clémence Goyens [1,*], Héloïse Lavigne [1], Antoine Dille [1] and Han Vervaeren [2]

[1] Operational Directorate Natural Environment, Royal Belgian Institute of Natural Sciences (RBINS), 29 Rue Vautierstraat, 1000 Brussels, Belgium
[2] R&D Department, De Watergroep, Vooruitgangstraat 189, 1030 Brussels, Belgium
* Correspondence: cgoyens@naturalsciences.be

Abstract: At the Blankaart Water Production Center, a reservoir containing 3 million m^3 of raw surface water acts as a first biologic treatment step before further processing to drinking water. Over the past decade, severe algal blooms have occurred in the reservoir, hampering the water production. Therefore, strategies (e.g., the injection of algaecide) have been looked at to prevent these from happening or try to control them. In this context, the HYperspectral Pointable System for Terrestrial and Aquatic Radiometry (HYPSTAR), installed since early 2021, helps in monitoring the effectiveness of these strategies. Indeed, the HYPSTAR provides, at a very high temporal resolution, bio-optical parameters related to the water quality, i.e., Chlorophyll-*a* (Chl_a) concentrations and suspended particulate matter (SPM). The present paper shows how the raw in situ hyperspectral data (a total of 8116 spectra recorded between 2021-02-03 and 2022-08-03, of which 2988 spectra passed the quality check) are processed to find the water-leaving reflectance and how SPM and Chl_a are derived from it. Based on a limited number of validation data, we also discuss the potential of retrieving phycocyanin (an accessory pigment unique to freshwater cyanobacteria). The results show the benefits of the high temporal resolution of the HYPSTAR to provide near real-time water quality indicators. The study confirms that, in conjunction with a few water sampling data used for validation, the HYPSTAR can be used as a quick and cost-effective method to detect and monitor phytoplankton blooms.

Keywords: earth observation; water quality; hyperspectral remote sensing; Belgium; Chlorophyll-*a*; suspended matter; cyanobacteria; inland waters; sustainable management; drinking water

Citation: Goyens, C.; Lavigne, H.; Dille, A.; Vervaeren, H. Using Hyperspectral Remote Sensing to Monitor Water Quality in Drinking Water Reservoirs. *Remote Sens.* **2022**, *14*, 5607. https://doi.org/10.3390/rs14215607

Academic Editors: Kim Calders, Bas van Wesemael, Trissevgeni Stavrakou, Dimitry van der Zande, Hans Lievens, Jean-Christophe Schyns and Joost Vandenabeele

Received: 31 August 2022
Accepted: 25 October 2022
Published: 7 November 2022

1. Introduction

The increasing occurrence of extreme summers, urban growth and socio-economical pressure challenges the safe-guarding and availability of surface and ground water quality. In 2021, the European Commission reported the need for actions to ensure the availability and sustainable use of freshwater resources [1]. Hence, there is an urgent need in extensive temporal and spatial water quality monitoring systems to provide scientific guidance for water resources management. Traditionally, water quality monitoring relied on sampling the water with a container and analyzing the water sample in the laboratory. However these discrete in time and spatially coarse sampling methods provide insufficient frequency and spatial coverage to capture fluctuations and trends in water quality or to investigate the effectiveness of remediation programs [2]. In recent years, significant advances have been made in online technologies to measure physical and chemical parameters using autonomous monitoring systems [3,4]. A large number of online sensors exists, each providing advantages and limitations.

Among the automated optical-based technologies, above-water visible and near-infrared optical radiometers have already shown to be a cost-effective solution for monitoring water quality and aquatic biogeochemical processes [5]. With adequate processing [6], the measured reflected light is processed as the water-leaving reflectance, also referred

to as the water color. Variations in spectral features seen in the water-leaving reflectance (i.e., in magnitude and shape) thus reflects variations in the inorganic, organic, particulate and dissolved materials present in the water, and, subsequently, provide insight into the water quality. With the development of hyperspectral radiometry, even finer-scale spectral features can now be detected [7,8], pushing the ability of optical sensors to address aquatic biodiversity, such as phytoplankton composition and abundance [9–11]. Palmer et al. [12] provide an overview of studies using hyperspectral data focusing on various inland water characteristics ranging from Chlorophyll-*a* (Chl_a) concentrations and the presence of organic and inorganic material to water turbidity/transparency and the identification and quantification of cyanobacteria blooms (e.g., [13–15]).

When mounted on automated pointing systems, above-water sensors provide water reflectance data at high temporal resolution and with very low manpower requirements. The development of such systems was mostly driven for the validation of satellite data [16–18]. However, with their very high temporal resolution data, autonomous systems may also be used for effective water quality monitoring. Cullen et al. [19] showed how one multispectral radiometer buoy could aid in monitoring and characterizing biological variability in surface waters over scales from minutes to months. Muller-Karger et al. [20] confirmed that long-term trends analysis requires measurements of short-term variability over long periods of time. Similarly, Song et al. [21] showed the feasibility of using hyperspectral remote sensing techniques as a rapid assessment tool for determining cyanobacterial abundance in drinking water systems.

In this context, the HYperspectral Pointable System for Terrestrial and Aquatic Radiometry (HYPSTAR) mounted on a pointable device, installed since early 2021, helps in monitoring the water quality over the Water Production Center (WPC) at Blankaart. The Blankaart WPC reservoir, located in Belgium 20 km from the Belgian coast (50.9888°N–2.8352°W), holds 3 million m^3 of water and acts as a first biologic treatment step before downstream processing. The Blankaart WPC is one of the main sources of drinking water for the coastal province of Belgium. During the last decade, the WPC has experienced several algal blooms. Due to their difficult removal from the water (more chemicals such as flocculants needed, clogged filters, etc.), algal blooms affect the production process of drinking water and force the water managers to rely on non-optimal water production planning. Knowing that Belgium is among the most water-scarce regions in Europe [1], preventing such situations is essential to ensure a sustainable drinking water supply.

The aim of the present study is (1) to demonstrate the capabilities of the HYPSTAR to provide reliable low-maintenance long-term reflectance measurements at very high temporal resolution, and (2) to investigate how the operational use of these continuous reflectance measurements may help in assessing the water quality. Here, we focus on two major water quality indicators, Chl_a and suspended particulate matter (SPM). The Chl_a concentrations provided by De Watergroep (i.e., water managers of the Blankaart WPC) from water sampling points allows us to validate and further improve the algorithms. In addition, to demonstrate the ability of hyperspectral sensors to retrieve more advanced water quality parameters, we investigated the potential of the HYPSTAR to detect phycocyanin, PC, an accessory pigment unique to freshwater cyanobacteria. However, the retrieval of PC is based on a limited number of match-ups between water sampling and HYPSTAR data and is therefore presented here as a feasibility study. Two extra measurements taken at Blankaart in 2019 and 2020 with the hyperspectral sensor PANTHYR [16] also complement the study to increase the number of validation data.

The Section 1 describes the HYPSTAR sensor and measured data as well as the processing used to estimate water-leaving reflectance. The water sampling data used for the validation of the Chl_a algorithms are described in Section 2.2. Section 2.3 describes the algorithms used for the retrieval of the water quality products, i.e., Chl_a and SPM. Improvements to those Chl_a algorithms are presented in Section 3.2. The retrieved long-term Chl_a and SPM time series together with the water sampling data and some concurrent satellite images are shown in Section 3.3. In Section 3.4, we investigate the potential to

detect phycocyanin with the HYPSTAR data. Finally, in Section 4, we discuss the possible improvements to further exploit the data and how the HYPSTAR water quality products could be used for operational water quality assessment in conjunction with satellite images.

2. Materials and Methods

2.1. Above Water Reflectance Data

2.1.1. HYPSTAR

A Hyperspectral Pointable System for Terrestrial and Aquatic Radiometry, HYPSTAR (www.HYPSTAR.eu, accessed on 14 October 2022), was installed at Blankaart WPC reservoir in January 2021 and continuously measures (except during short periods of downtime for maintenance) the upwelling and downwelling radiance and downwelling irradiance during daylight (7 a.m. till 6 p.m. local time). The HYPSTAR installed at Blankaart (Figure 1) measures the reflected light within the visible and near-infrared (VNIR) spectral range (380–1020 nm) with a spectral sampling and resolution of 0.5 and 3 nm, respectively, and a field of view of 2°. The HYPSTAR is mounted on a pan and tilt unit allowing commands to be received from the host system and to return measurements according to the defined measurement protocol (i.e., viewing geometries, number of scans, radiance or irradiance measurements, etc.). The system also includes a GPS and embedded camera to visualize the target and sky conditions for visual inspection. A true color Sentinel-2B image and the panchromatic GEOEye image acquired over the reservoir show the octagonal shape of the 800 m-diameter drinking water reservoir (see Figure 1). The reservoir has a concrete wall of 400 m built from its north-east edge to its center. The HYPSTAR is deployed on this wall, 30 m from the external border. The HYPSTAR has been developed in the frame of the H2020 HYPERNETS project (www.hypernets.eu, accessed on 14 October 2022), and is part of the HYPERNETS network [22].

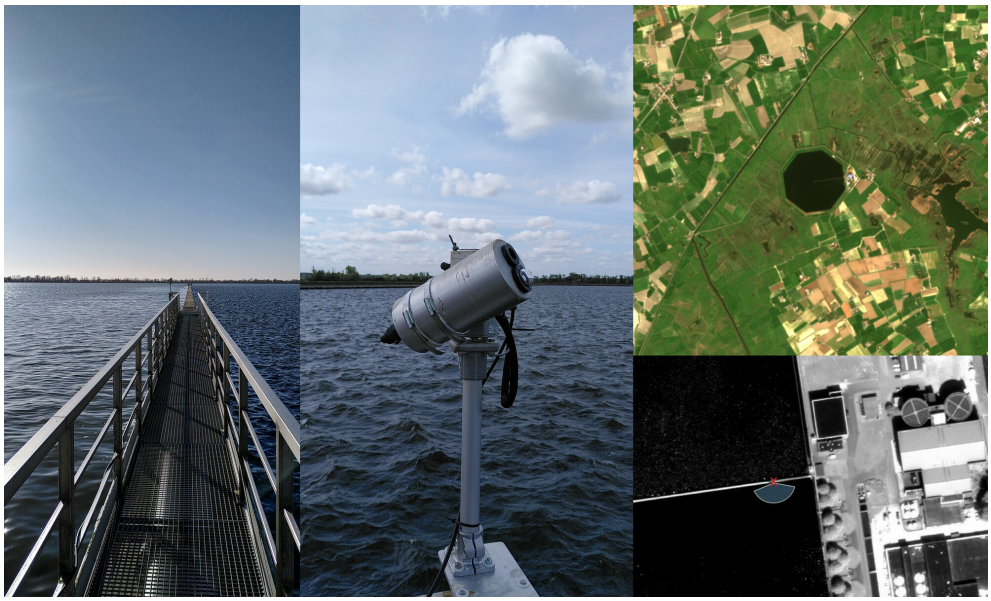

Figure 1. View from the north-east edge of the concrete wall in the Blankaart drinking reservoir (**left**), close-up on the HYPSTAR installed along the railing 30 m from the border edge (**middle**), and true color Sentinel 2A image acquired on 2021-02-04 and processed with ACOLITE [23] with the Blankaart reservoir in the center of the image (**top right**) and the panchromatic GEOEye image acquired on 2019-05-24 (**bottom right**). A red cross indicates the location of the sensor (50.9888°N–2.8352°W). The blue semi-circle shows the orientation of the sensor during the day.

2.1.2. Acquisition Protocol and Data Processing

The above-water approach includes measurements from above-water radiometers for $L_d(\lambda, 180-\theta, \Delta\phi, \theta_0)$, $L_u(\lambda, 180-\theta, \Delta\phi, \theta_0)$ and $E_d(\lambda)$, the downwelling radiance, upwelling radiance and downwelling irradiance, respectively. In the absence of sun glint,

(near-) simultaneous $L_d(\lambda, 180-\theta, \Delta\phi, \theta_0)$ and $L_u(\lambda, 180-\theta, \Delta\phi, \theta_0)$ measurements allow the evaluation of the water-leaving radiance, $L_w(\lambda)$ as follows:

$$L_w(\lambda, 180-\theta, \Delta\phi, \theta_0) = L_u(\lambda, 180-\theta, \Delta\phi, \theta_0) - \rho_F(\lambda, \theta, \Delta\phi, \theta_0, ws, E) L_d(\lambda, 180-\theta, \Delta\phi, \theta_0) \quad (1)$$

The term ρ_F is the air–water interface reflectance coefficient expressed as a function of viewing geometry, i.e., θ, $\Delta\phi$, and sun zenith angle θ_0, and environmental factors, E. When the water surface is perfectly flat, ρ_F is the Fresnel reflectance and the environmental factor E only depends on the relative refractive index of the air–water interface. When the water is not perfectly flat, ρ_F needs to account for the geometric effects of the wave facets created by the roughened water surface. Wave facets change the water surface geometry and thus (1) the upwelling rays by changing the relative geometry between the illumination and viewing direction, as well as (2) the contribution of the sky and sun glint to $L_u(\lambda, 180-\theta, \Delta\phi, \theta_0)$. After normalization by $E_d(\lambda)$, $L_w(\lambda)$ becomes the remote sensing reflectance, $R_{rs}(\lambda)$ (expressed in sr^{-1}), or, when multiplied by π, the water-leaving reflectance, $\rho_w(\lambda)$ (dimensionless). These are the standard input for most optical models used to derive bio-geochemical products.

Numerous measurement protocols exist for the correction of the air–water interface reflectance for above-water acquisitions (e.g., [6] and references therein). However, the present study does not intend to provide an inter-comparison of these methods and follows, therefore, the approach adopted by NASA [24] and IOCCG [25] for the measurement protocol and data processing. Radiometer measurements are taken with the HYPSTAR in a defined set of geometries called a sequence. Each geometry in a sequence is called a series, composed of a set of repeated scans that are averaged. Thus, a single sequence results in one measurement of water-leaving reflectance. A sequence was taken every 15 to 30 min during daylight and contained the following series:

1. Three scans of $E_d(\lambda, \theta = 180°, \Delta\phi = +/-90°)$;
2. Three scans of $L_d(\lambda, \theta = 140°, \Delta\phi = +/-90°)$;
3. Six scans of $L_u(\lambda, \theta = 40°, \Delta\phi = +/-90°)$;
4. Three scans of $L_d(\lambda, \theta = 140°, \Delta\phi = +/-90°)$;
5. Three scans of $E_d(\lambda, \theta = 140°, \Delta\phi = +/-90°)$.

2.1.3. Data Processing

Data are processed using the Hypernets Processor [22], which is fully accessible via (https://github.com/HYPERNETS/hypernets_processor, accessed on 14 October 2022). The first step in the processor is to check the quality of the raw radiance and irradiance data and the blacks. Next, raw scans are corrected for darks and calibrated to irradiance and radiance scans. For the computation of the water reflectance, the HYPERNETS processor includes the RHYMER component (i.e., "Reliable processing of HYperspectral MEasurement of Radiance"). RHYMER provides all the required functions to process the above-water measurements and is written as such that it can easily welcome any additional look-up tables, processing functions, and/or quality flags. Before averaging per series, RHYMER first assigns flags to each scan showing a temporal jump, with the previous and following scan, of more than 25 at 550 nm. Next, RHYMER parses the cycle, i.e., it separates upwelling and downwelling radiance, investigates if all required angles are present and if there are coincident upwelling and downwelling radiance measurements for the retrieval of the water-leaving radiance. Since the irradiance and radiance measurements have a slight shift in wavelength, a spectral interpolation is first performed between radiance and irradiance spectra. Next, $E_d(\lambda)$ and $L_d(\lambda)$ scans are averaged per series and temporally interpolated to $L_u(\lambda)$ scans. For the computation of the water-leaving reflectance, the reflectance factor ρ_F is retrieved from the look-up table of [26] using as input the solar zenith angle, viewing zenith angle, relative azimuth angle between sun and sensor, and the wind speed, at 10 m above the sea surface.

In the present study, wind speed is taken from a nearby station, i.e., the VLINDER station located at Blankaart. The VLINDER data, (www.vlinder.ugent.be, accessed on 14 October 2022) [27], provide near-real-time weather data including temperature, rainfall, wind speed, and wind direction.

To ensure quality reflectance data and discard any suspect spectra (e.g., noisy or non-water spectra, high variation in illumination during the sequence, and/or inconsistency between radiance and irradiance measurements during the sequence), three additional quality checks are used. A spectrum is discarded if one of these conditions are met:

- Filter 1: the ratio of $L_u(\lambda)/E_d(\lambda)$ between 800 and 950 nm is greater than 0.025 sr^{-1};
- Filter 2: the NIR similarity correction factor, $\epsilon(720,780)$, exceeds a given threshold (with $\epsilon(720,780)$ defined by Equation (8) in [28]);
- Filter 3: negative reflectance values between 400 and 900 nm.

The first filter relies on the fact that the water radiance is expected to be very low in the 800–950 nm spectral range as most of the water absorbs in these wavelengths. As observed by Groetsch et al. [29], applying filter 1 removes most of the spectra affected by foam-caps or surface scum. We found that this empirical threshold also removed most of the suspect spectra in our dataset without considering inaccuracies in the data processing.

The second filter was used to remove spectra for which we suspect erroneous processing. According to Ruddick et al. [30], the shape of the NIR spectrum is mainly determined by the pure water absorption and is thus invariant. Hence, for waters following this theory, $\epsilon(720,780)$ is the residual error when the data processing results in an inaccurate correction for the presence of high sun glint. Despite the 90° relative azimuth between sun and sensor, $\Delta\phi$, during acquisition attempts to avoid sun glint, over wind-roughened surfaces, sun glint may still be present in the field of view of the sensor. Therefore, spectra for which the estimated $\epsilon(720,780)$ exceeds a given threshold are considered as inaccurately processed and removed for further data analysis. The threshold (see Section 3.1) of $\epsilon(720,780)$ is defined based on a visual inspection of the removed and remaining spectra.

The last filter removes the negative reflectance spectra. Negative reflectance often results from an inaccurate removal of the air–water interface reflectance. The estimation of ρ_F in Equation (1) is indeed often a source of error when, among other things, the wave slope distribution at the surface is unknown and/or there are above-water optical perturbations [6]. The filters suggested here present a good compromise between the number of data to retain (i.e., allowing a high temporal resolution time series) and the autonomous quality assessment of the data (i.e., essential for autonomous systems recording very high amounts of data).

2.2. Validation of Data

2.2.1. Chl_a Concentrations

Surface water was sampled with a 5 L bucket on irregular days by the water managers for monitoring the water quality. Although it was not meant to be used for the validation of the water quality products from the HYPSTAR, it appeared to be very relevant as the sampling was conducted from the same platform where the HYPSTAR was installed. After sampling, Chl_a concentrations were determined with a spectrophotometric method, 10200 H [31].

In total, we found 43 Chl_a concentrations sampled during the time interval of the HYPSTAR deployment (i.e., since January 2021).

2.2.2. Counting Procedure for Cyanobacteria and Diatoms

For the manual counting of the algae, the sampling protocol and preparation followed the "Water Sampling, Measurement and Analysis Compendium (WAC)" from the Flemish Government [32] and the European standard EN 15204 [33].

2.3. Algorithms for Water Quality Products

2.3.1. Chl_a

Both multispectral [14] and hyperspectral [34] red-edge approaches are tested and compared with the water sampling retrieved Chl_a. The red-edge spectral region is well-suited for detecting Chl_a in turbid and eutrophic waters thanks to the combination of the high Chl_a absorption around 672 nm and its strong scattering around 705 nm [35]. Blue-green band ratio algorithms and quasi-analytical algorithms, often referred to as QAA [36], or the generalized inherent-optical-properties inversion [37] are less suited for these inland waters because of the significant influence of the dissolved and particulate material in blue and green bands. The quasi-analytical algorithms were generally developed for clear waters to moderately turbid waters.

Among the wide variety of red-edge-based algorithms, the algorithm proposed by Simis et al. [14] (referred to hereafter as the SIMIS algorithm) was selected because it is very close to the semi-empirical algorithm introduced by Gons [38]. This algorithm is also associated with a phycocyanin algorithm which is assessed here to monitor cyanobacteria blooms. The algorithm suggested by Ruddick et al. [34], also referred to as the "Chlorophyll a Retrieval using an Adaptive Two-band" algorithm (referred to hereafter as the CRAT algorithm), has been selected to investigate the benefits of the hyperspectral resolution. Although the CRAT algorithm is only based on two spectral bands, the spectral position of the second band varies from one spectra to another and can only be determined from hyperspectral data. Both algorithms assume (1) a constant back-scattering coefficient, b_b, in the red and NIR, (2) a negligible absorption from colored dissolved organic matter (CDOM) and non-algal particles compared with water absorption (a_w) at 672 nm, 704 nm and 750 nm and to Chl_a absorption at 672 nm, and (3) negligible absorption by phytoplankton at 704 nm and 750 nm.

With the SIMIS algorithm, Chl_a concentrations are estimated from the Chl_a absorption at 665 nm, $a_{Chl}(665)$, as follows:

$$a_{Chl}(665) = \frac{\frac{\rho_w(709)}{\rho_w(665)}(a_w(709) + b_b) - b_b - a_w(665)}{\gamma} \quad (2)$$

where γ is a factor applied to correct underestimation due to the hypothesis of negligible CDOM and non-algal particulate absorption. Simis et al. [14] estimated γ to be equal to 0.68 for the Ijselmeer. However, because this parameter is very regional, it is set to 1 in the present study, as suggested by Gons [38]. b_b is calculated from $\rho_w(779)$ as proposed in Gons et al. [39] and the pure-water absorption coefficients, $a_w(\lambda)$, are retrieved from Buiteveld et al. [40]. Chl_a absorption is then converted into Chl_a concentration using the Chl_a-specific absorption coefficient, $a^*ph(665)$:

$$Chl_a^S = \frac{a_{Chl}(665)}{a^*ph(665)} \quad (3)$$

$a^*ph(\lambda)$ is the absorption coefficient of phytoplankton per unit of Chl_a concentration. Simis et al. [14] suggests a constant $a^*ph(665)$ equal to 0.0153 m^2m/g for the IJselmeer.

With the CRAT algorithm, Chl_a is calculated differently for each spectrum as:

$$Chl_a^C = \frac{a_w(\lambda_2) - a_w(\lambda_1)}{a * ph(672)} \quad (4)$$

where λ_2 is selected individually in the 704–740 nm interval as the wavelength at which the reflectance is equal to the reflectance at the red Chl_a absorption peak (i.e., $\rho_w(\lambda_2) = \rho_w(\lambda_1)$). λ_1 is equal to 672 nm [34].

Compared with the SIMIS algorithm (and similar algorithms, see references in [14]), the CRAT is based on a subtraction which avoids the calculation of b_b. In addition, residual absorption from CDOM and non-algal particles are also partially corrected [34].

$a * ph(\lambda)$ values are known to vary as a function of a variety of factors, such as phytoplankton-specific pigment composition or the water trophic state [41]. As mentioned by Bramich et al. [42], and references therein, the use of a varying $a^* ph(\lambda)$ is therefore expected to improve the Chl_a concentration estimates, in particular for the lowest and highest concentrations. Therefore, Bricaud et al. [41] recommended using a power function of the form:

$$a^* ph(\lambda) = A Chl_a^{-B} \quad (5)$$

where A and B are wavelength-specific coefficients (A reflects $a^* ph(\lambda)$ per Chl_a unit while the B exponent reflects the deformations of $a^* ph(\lambda)$ with an increase in Chl_a concentrations). Locally tuned A and B coefficients have already been used by numerous studies (e.g., [43,44]). We therefore also analyzed how using a varying $a^* ph(\lambda)$ could improve the accuracy of Chl_a^S and Chl_a^C by deriving a linear regression between the logarithm of $a^* ph(\lambda)$ and logarithm of Chl_a from the water sampling, Chl_a^W. Hence, the slope of the linear regression is equal to B in Equation (5) and the intercept to $\log(A)$.

Ultimately, we compared the accuracy of Chl_a^S and Chl_a^C with a constant $a^* ph(\lambda)$ and with a varying $a^* ph(\lambda)$ (as in Equation (5)). To evaluate their performance, we used the following metrics.

- The Root Mean Square Error (RMSE), which measures the scatter of the data from the regression line (units in µg/L);
- The slope (S) and intercept (I) of the least squares regression to detect systematic multiplicative or additive biases;
- The Mean Absolute Percentage Error ($MAPE$, unsigned and units in %) between the HYPSTAR-retrieved Chl_a, Chl_a^C or Chl_a^S, and water-sampling-retrieved Chl_a and Chl_a^W, for a total number of samples n. $MAPE$ is calculated as follows:

$$MAPE = 100 \times \frac{1}{n} \Sigma_{i=1}^{i=n} \frac{|Chl_a^{C,S} - Chl_a^W|}{Chl_a^W} \quad (6)$$

- The $BIAS$, to assess the systematic errors in the algorithm outputs (units in µg/L), calculated as follows:

$$BIAS = \frac{1}{n} \Sigma_{i=1}^{i=n} (Chl_a^{C,S} - Chl_a^W) \quad (7)$$

2.3.2. *SPM*

For the computation of SPM, the algorithm from Nechad et al. [45] was used with the measured water-leaving reflectance at 700 nm as follows:

$$SPM = \frac{A^{N2010} \rho_w(700)}{1 - \frac{\rho_w(700)}{C^{N2010}}} \quad (8)$$

where A^{N2010} and C^{N2010} are constant values (i.e., 445.11 and 1.13, respectively) taken from Table 1 in [45]. This algorithm has already been used and validated by numerous studies (e.g., [46,47]).

Table 1. Constant A and B values estimated in the present study with the SIMIS algorithm and found in the literature [41,44] for λ equal 665 and 672 nm.

	λ = 665 nm		**λ = 672 nm**	
	A	**B**	**A**	**B**
SIMIS	0.0537	−0.3897	–	–
Paavel	0.0311	−0.2711	0.0339	−0.2488
Bricaud	0.0150	−0.1333	0.0197	−0.1530

2.3.3. Cyanobacteria

Since the match-ups between water sampling points and HYPSTAR reflectance data were not sufficient to properly validate or design a cyanobacteria algorithm (only two match-ups), we limited our results to the evaluation of several indexes. We also complemented the dataset with two extra PANTHYR measurements [16] taken at Blankaart during large cyanobacteria blooms in 2019 and 2020.

Several indexes have been developed from cyanobacteria spectral specificities due to PC absorption and cyanobacteria fluorescence anomalies. Using an analytical algorithm, Simis et al. [14] proposed calculating the concentration in PC from its absorption at 620 nm and after correction for water and Chl_a absorption (i.e., estimated with the SIMIS algorithm in Section but using the 620 nm reflectance band). This first index, referred to as $CI1$, is estimated as follows:

$$CI1 = \frac{\left[\frac{\rho_w(709)}{\rho_w(620)}(a_w(709) + b_b)\right] - b_b - a_w(620)}{\delta} - \epsilon^{665-620} \times a_{Chl}(665) \quad (9)$$

with $\epsilon^{665-620}$ being the conversion factor from $a_{Chl}(665)$ to $a_{Chl}(620)$ (equal to 0.24, [14]), and δ being the correction factor similar to γ in Equation (2). In the present study, δ is set to 1 for the same reasons as mentioned above.

The second index, referred to as $CI2$, is the band ratio between $\rho_w(600)$ and $\rho_w(700)$ as suggested by Mishra et al. [15]:

$$CI2 = \frac{\rho_w(700)}{\rho_w(600)} \quad (10)$$

These bands were chosen for their low variability (minimum reflectance at 700 nm) and for the absence of influence of Chl_a absorption at 600 nm while phycocyanin is still absorbing. Hence, the higher the index, the higher the probability of cyanobacteria presence.

The third index, referred to as $CI3$, is proposed by Wynne et al. [48] and is similar to a fluorescence line height equation with a focus on the spectral shape around 681 nm. According to the authors, a deficit of fluorescence at 681 nm is expected in the presence of cyanobacteria compared with other phytoplankton groups. A negative value for $CI3$ is expected in the presence of cyanobacteria whereas a positive value is expected in the absence of cyanobacteria.

$$CI3 = \rho_w(681) - \rho_w(665) - [\rho_w(709) - \rho_w(665)][\frac{681 - 665}{709 - 665}] \quad (11)$$

3. Results

3.1. Water-Leaving Reflectance

The dataset consists of 8116 spectra measured in the period 2021-01-27 to 2022-08-03 (Figure 2). A first quality check is performed to filter out the suspect data (see filter 1 in Section 2.1.2), reducing the number of valid data to 7933. Data with $\epsilon(720, 780)$ greater than 0.005 (filter 2) are then removed, leaving 6535 spectra. The threshold of 0.005 is large enough to retain the optically complex waters and severe enough to remove non-water or glint-affected spectra. Finally, all spectra showing (non-physical) negative values between 400 and 900 nm are removed, leaving 2988 individual measurements in the dataset, ranging from 2021-02-03 to 2022-08-03. More data are removed during the winter (high wind, rain, low illumination, changing weather, etc.) with the number of sequences retained in December, January and February being 38, 74 and 89, respectively. In the summer (June, July and August) the number of sequences varies between 622 and 307 sequences per month.

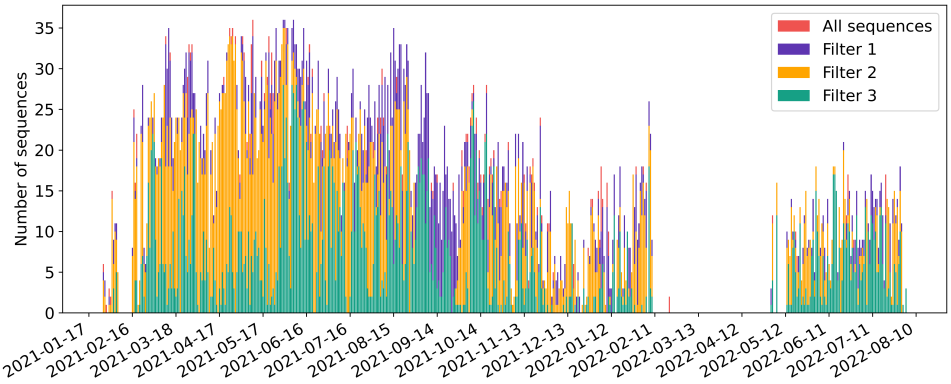

Figure 2. Number of valid sequences taken each day ("All sequences"), and the remaining sequences after removing the spectra that do not satisfy the following filters: (1) Filter 1: $L_u(\lambda)/E_d(\lambda)$ between 800 and 950 nm > 0.025 sr^{-1}; (2) Filter 2: $\epsilon(720, 780) > 0.005$; and (3) Filter 3: removing negative reflectance data in the 400–900 nm range. Note that instrument was in maintenance and recalibration in February–April 2022.

Figure 3 shows the daily mean reflectance of all the retained sequences over the different seasons. As expected, all spectra show typical spectral shapes for inland waters, i.e., low reflectances in the blue compared with reflectances in the green and red spectral range [49]. The magnitude of the reflectance value is higher in the winter season compared with the rest of the year. This is especially visible for the 500–600 nm range and results from higher particle concentrations in the winter months or the resuspension of sediments in the reservoir due to high winds. Several distinguishing finer spectral features are also observed. First, the so called red-edge reflectance (i.e., ∼680–750 nm) is visible, essentially in spring and summer. This increase in reflectance can be associated with increasing Chl_a concentrations [50]. Likewise, a clear U-shape is present for many spectra in the 650–710 nm range in spring and summer, but less in winter and autumn. This U-shaped feature is a typical indication of high particle scattering bounded by high pigment absorption ([49], and references therein). These spectra are expected to present high Chl_a concentrations and the possible presence of cyanobacteria [48,51].

3.2. Chl_a Retrieval

Out of the 43 water sampling points taken between 2021-01-27 and 2022-08-03, 27 Chl_a^W concentrations were taken during a HYPSTAR reflectance spectrum (i.e., passing the quality check mentioned above) (see Figure 4). Concentrations range from 1.5 µg/L to 39.4 µg/L. As mentioned, a U-shaped spectra around 650–670 nm is clearly visible for the higher Chl_a concentrations, typical for high phytoplankton absorption. Note, however, that absorption at 670–675 nm is not only related to Chl_a but may also be related to suspended particulate absorption [34]. Similarly, higher Chl_a concentrations tend to show an increase in the reflectance peak around 710–720 nm and 555 nm.

Figure 5 shows the accuracy of the retrieved Chl_a concentrations using the CRAT and SIMIS algorithms, respectively. Note that the CRAT algorithm using the wavelength range 704–740 nm is not expected to perform well for Chl_a values outside the ∼10–100 µg/L range, as reported by Ruddick et al. [34]. Therefore, statistics are limited here for Chl_a concentration within this range, reducing the number of match-ups between water sampling and HYPSTAR data to 11.

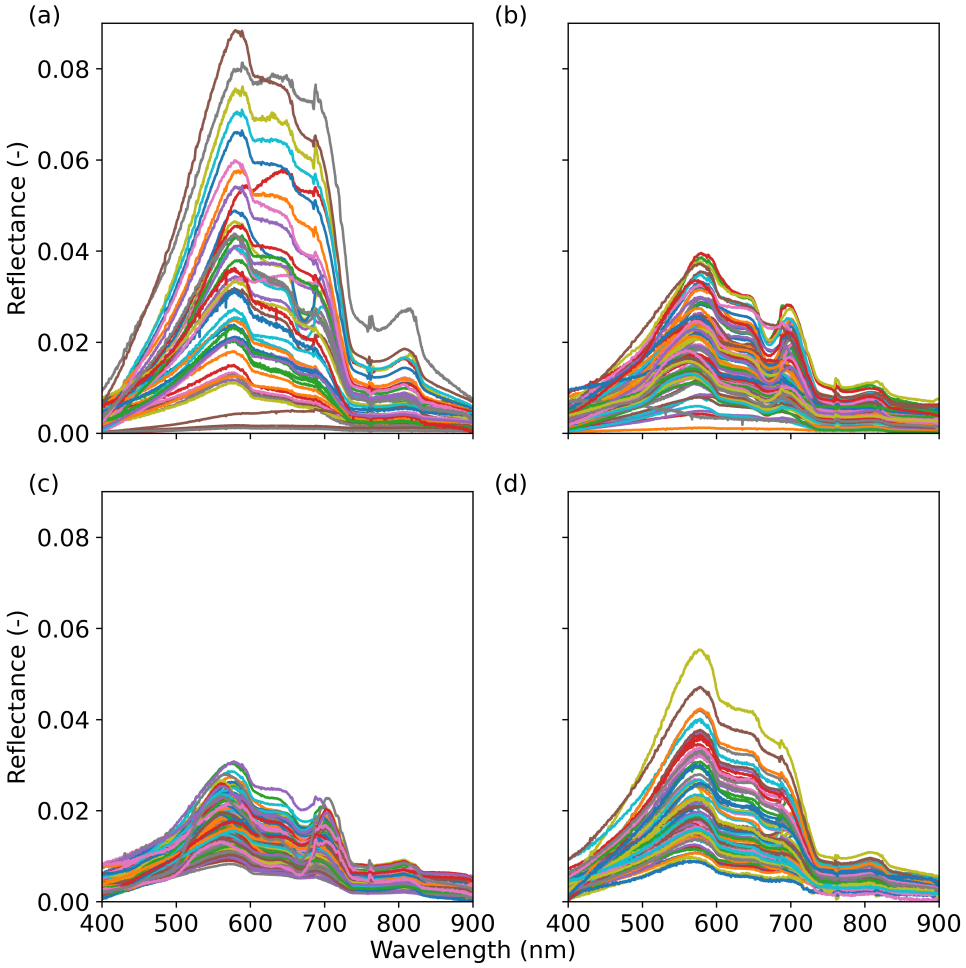

Figure 3. Reflectance spectra measured at Blankaart and averaged per day (to maximize visibility, each day has a different color) for the winter (December, January and February) (**a**), spring (March, April and May) (**b**), summer (June, July and August) (**c**), and autumn (September, October and November) (**d**).

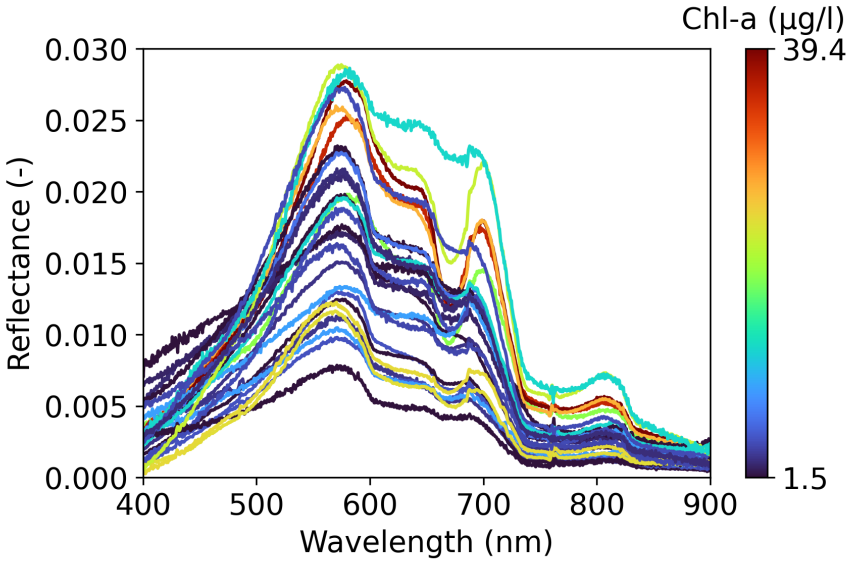

Figure 4. Water reflectance spectra taken with the HYPSTAR and coincident Chl_a concentrations from the water sampling measurements.

An $a^*ph(672)$ of 0.0177 ± 0.00151 m^2mg^{-1} is found to be the most appropriate for the CRAT algorithm. An $a^*ph(665)$ of 0.01995 ± 0.00165 m^2mg^{-1} performs better for the SIMIS algorithm. These values are in line with what is found in the literature (i.e., [34] found an $a^*ph(672)$ of 0.0205 m^2mg^{-1} for the IJssel lagoon with the CRAT algorithm, and [14] an $a^*ph(665)$ between 0.0153 and 0.0203 m^2mg^{-1} for different lakes with the SIMIS algorithm).

The RMSEs are 8.20 µg/L and 5.61 µg/L for the CRAT and SIMIS algorithm, respectively. For the CRAT algorithm, we observe a MAPE of 28.5 % and a BIAS of 1.27 µg/L. For the SIMIS algorithm, MAPE and BIAS are 75.6% and 0.16 µg/L, respectively. Both algorithms tend to overestimate the lower Chl_a concentrations and underestimate the higher concentrations. The minimum Chl_a concentration retrieved with the CRAT algorithm is 12.14 µg/L (Figure 5). Using an $a^*ph(672)$ of 0.0177 m^2mg^{-1} and with λ_1 equal to 672 nm and λ_2 in the 704–740 nm wavelength range, the retrieval range of the CRAT algorithm is between 12.14 µg/L and 119.56 µg/L Chl_a (i.e., between $[a_w(704) - a_w(672)]/0.0177$ and $[a_w(740) - a_w(672)]/0.0177$ with $a_w(\lambda)$ equals 0.415, 0.6303 and 2.5319 m^{-1}, at 672, 704 and 740 nm, respectively).

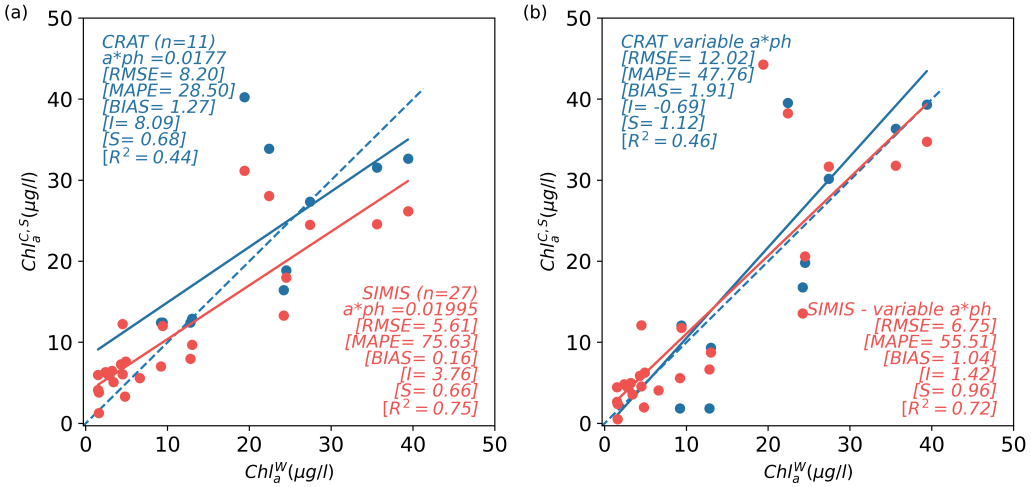

Figure 5. Comparison between Chl_a products from the water sampling (Chl_a^W) and when computed with the SIMIS algorithm (Chl_a^S, red dots) and CRAT algorithm (Chl_a^C, blue dots) using a fixed $a^*ph(\lambda)$ (**a**) and variable $a^*ph(\lambda)$ (**b**), as shown in Figure 6. Plain lines are the regression lines for each algorithm (red and blue plain lines for the SIMIS and CRAT algorithm, respectively) with I and S being the intercept and slope, respectively. Statistics are computed on 11 points for CRAT and 27 points for SIMIS. Dashed blue line is the 1:1 line.

The value of $a^*ph(\lambda)$ decreases from 0.08 to 0.006 m^2/mg at the red Chl_a absorption peak (i.e., 665 nm, Figure 6a). At 672 nm, $a^*ph(\lambda)$ ranges from approximately 0.04 to 0.006 m^2/mg. Note that the high $a^*ph(\lambda)$ values should not be considered as these correspond to Chl_a concentrations below the retrieval range (i.e., see points before gray dashed line in Figure 6b). Table 1 provides the values for A and B in Equation (5) when retrieved with the SIMIS algorithm. For comparison, A and B values reported by Bricaud et al. [41] and Paavel et al. [44] are also added. Since the number of match-ups with Chl_a concentrations above 8 µg/L is limited (i.e., 11 out of 27), we used the A and B values from Paavel et al. [44] for the CRAT algorithm. These constant values for A and B were estimated with 155 water samples taken in different lakes (including cyanobacteria-dominated lakes) for Chl_a concentrations ranging from 3 to 315 µg/L [44]. Overall, this relationship fits well with our data for Chl_a concentrations above 10 µg/L (see Figure 6b).

For the SIMIS algorithm, the performance of the algorithm increases when using a variable $a^*ph(\lambda)$ (Figure 5). MAPE and BIAS decrease to 55.51 % and 1.04 µg/L, respectively. For the CRAT algorithm, the MAPE and RMSE increase, but the regression line is closer to the 1:1 line (slope and intercept approaches 1 and 0, respectively).

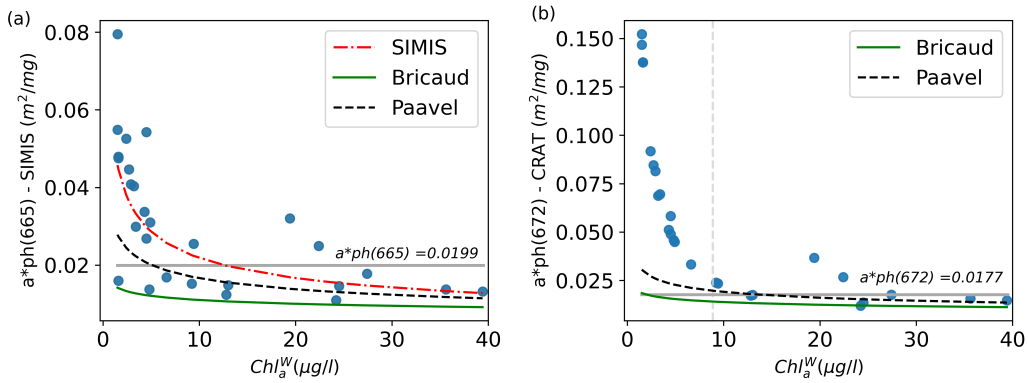

Figure 6. Dependence of $a^*ph(665)$ (**a**) and $a^*ph(672)$ (**b**) on Chl_a concentrations from the water sampling (Chl_a^W) for the SIMIS and the CRAT algorithm, respectively. Equations found by [41,44] are also added (see color legend). Horizontal gray lines show the fixed $a^*ph(\lambda)$. Dashed vertical gray line shows the limit at 8 µg/L for the application of the CRAT algorithm (**b**).

3.3. Chl_a and SPM Time Series

The HYPSTAR-retrieved Chl_a^S and Chl_a^C follow closely the water sampling Chl_a^W concentrations (Figure 7), although Chl_a^S and Chl_a^C show higher peaks in Chl_a concentrations relative to the water sampling data. These peaks may be explained by (1) the high temporal resolution of the HYPSTAR data depicting Chl_a variations that are omitted by the water sampling data, (2) failure of the quality check of the reflectance data to remove some non-valid or suspect reflectance spectra, and/or (3) the erroneous estimation of $a^*ph(\lambda)$ at high Chl_a concentrations. As mentioned in Section 3.1 and illustrated in Figure 3, we indeed observe overall lower Chl_a concentrations in autumn (although some high Chl_a values are seen early September) and relatively higher values in the spring and summer. Note that during the spring and summer months, measures are taken to prevent algal blooms (i.e., the injection of algaecide) within the reservoir. This could explain why the Chl_a concentrations are limited, in particular in the summer of 2021, and why in some cases sudden drops in Chl_a concentrations are observed (e.g., in July 2022).

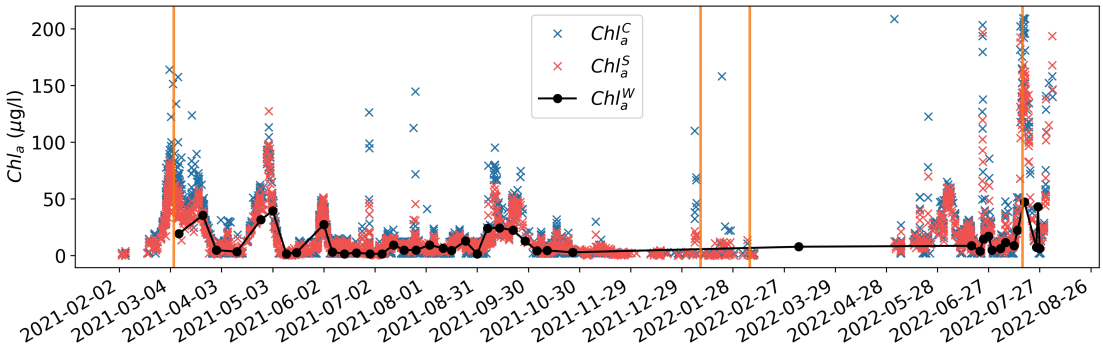

Figure 7. Time series of HYPSTAR-retrieved Chl_a concentrations using CRAT and SIMIS algorithms (blue and red dots, respectively), and Chl_a concentrations measured from the water sampling points (black) between January 2021 and August 2022. Orange vertical bars point to specific dates discussed in the text and reported in Table 2, i.e., 2021-03-06, 2022-02-07, 2022-01-10, and 2022-07-17.

Figure 8 shows the Chl_a values over a shorter time period and the corresponding reflectance spectra for the given Chl_a values. A peak in Chl_a concentration was observed around 2021-04-30 (Figure 8a). Afterwards, the Chl_a concentration slowly decreased until 2021-05-05 and remained low until the end of May. In early June, the Chl_a concentration increased again up to ~40 µg/L. Spectra associated with higher Chl_a values (i.e., 2021-05-03

and 2021-06-02) can clearly be distinguished by their pronounced reflectance peaks at 700 nm and deep U-shaped features between 640 and 700 nm (Figure 8b). Differences in spectral shapes between 2021-05-03 and 2021-06-02 may be related to the higher abundance of diatoms on 2021-05-03 (i.e., 29.8 mm^3/L compared with 7.8 mm^3/L on 2021-06-02). On 2021-05-03, we also observe two absorption features around 490 nm and 620 nm typical for Chl_c and the possible presence of PC. However, according to the water sampling data, there was no presence of cyanobacteria at that time.

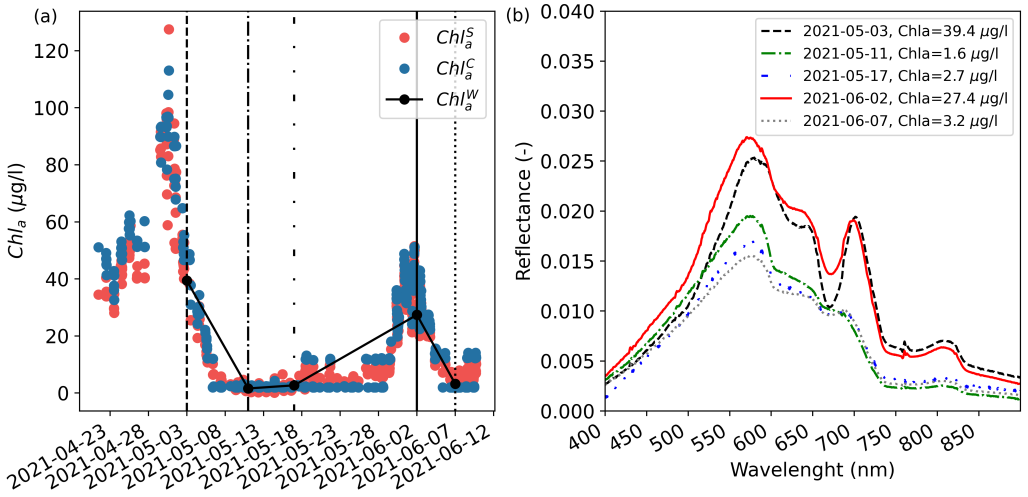

Figure 8. Zoom of Figure 7 between 2021-04-23 and 2021-06-12 (**a**) and reflectance spectra with corresponding Chl_a concentrations retrieved with the water sampling points (**b**).

SPM values range from 0 to 30 g/m^3 with some peaks reaching 60 g/m^3 (Figure 9). There were no coincident data with the water sampling points for *SPM*. However, for both peaks in *SPM*, i.e., around 2022-01-09 and 2022-02-07, a Landsat-9 OLI and Sentinel 2B-MSI image confirmed the relatively high plume of sediments along the southern side of the wall (see Figure 10).The timing of these sediment plumes also corresponded to storm events (see high gustwind in Figure 9). Storm events may induce high sediment concentrations in the water that is pumped into the reservoir, and/or the resuspension of the sediments present in the bottom of the water reservoir. The latter explanation may be more valid since during heavy storms, and especially during flooding, the intake of water into the reservoir is stopped.

Relatively high values of reflectance, in particular in the red and NIR spectral range, are observed for those two dates (Figure 10). *SPM* values retrieved from the reflectance spectra taken the same day (i.e., 2022-02-07) or the day before (i.e., 2022-01-10) are also relatively high, with concentrations of 27.59 and 33.07 g/m^3. For comparison, two spectra corresponding to high Chl_a values (see Figure 7) and low *SPM* values (see Figure 9), i.e., 2021-03-06 and 2022-07-17, are also shown (Figure 10). Table 2 reports, for these four dates, the number of sequences per day (after quality check), the estimated *SPM* values, and the retrieved Chl_a^S and Chl_a^C concentrations.

Table 2. Mean and standard deviation of *SPM* and Chl_a concentrations retrieved with the CRAT and SIMIS algorithm on different dates (see orange bars in Figures 7 and 9, and associated reflectance spectra in Figure 10).

Date	Numb. Seq.	SPM (g/m^3)	Chl_a^C (µg/L)	Chl_a^S (µg/L)
2021-03-06	5	8.78 ± 0.07	86.88 ± 3.47	60.60 ± 1.85
2022-02-07	18	27.59 ± 2.92	–	0.14 ± 0.12
2022-01-10	2	33.07 ± 4.74	–	2.52 ± 0.13
2022-07-17	13	7.75 ± 0.57	207.25 ± 5.5	142.94 ± 11.71

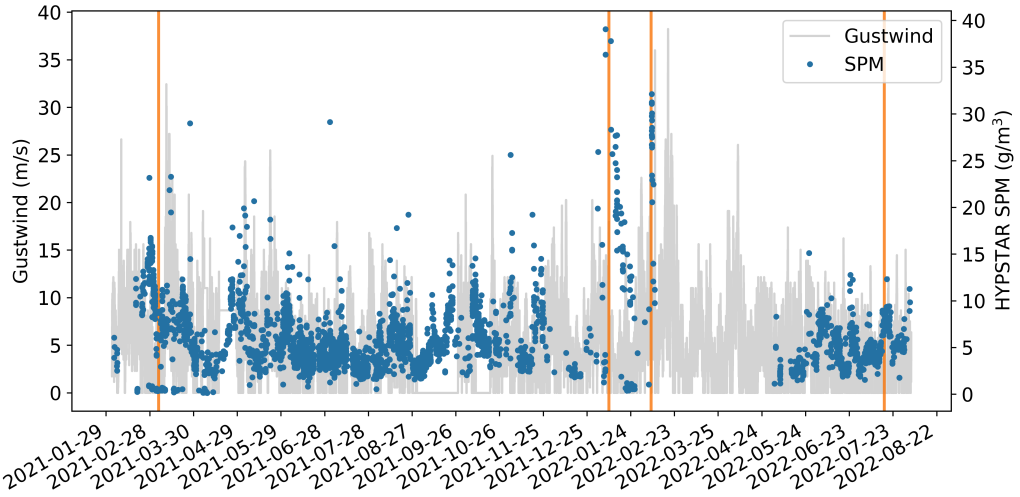

Figure 9. Time series of SPM (g/m^3) retrieved with HYPSTAR using the algorithm of Nechad et al. (2010) with the 700 nm band, and gustwind (m/s) (retrieved from the VLINDER station at Blankaart) from January 2021 to August 2022.

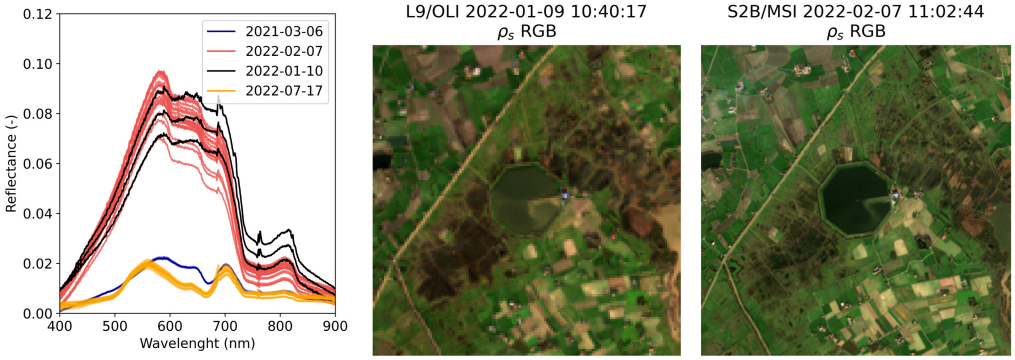

Figure 10. Spectra for the different dates given with the orange vertical bars in Figures 7 and 9 and Landsat-9 OLI RGB image and Sentinel-2B MSI RGB image processed with ACOLITE [23] taken on 2022-01-09 and 2022-02-07, respectively.

3.4. Cyanobacteria Detection: A Feasibility Study

To evaluate the different PC indexes, extra hyperspectral remote sensing data, acquired by a PANTHYR sensor [16], were also analyzed as they provided some concomitant water reflectance spectra during large cyanobacteria bloom events. Indeed, in 2021–2022, Blankaart reservoir experienced only small cyanobacteria bloom events with a maximum of 5 µg/L observed from water samples on 2021-09-06 and 2021-09-21. Figure 11 displays water reflectance spectra and the second derivative from a diatom bloom (2021-05-02) and from cyanobacteria blooms (2019-08-01, 2020-06-15 and 2021-09-06, see also Table 3). From these spectra, the different indexes are calculated.

$CI1$, as suggested by [14], shows increasing values when the concentration of cyanobacteria increases. In particular, when cyanobaceria concentration increases from 0 to 4.70 µg/L, CI increases from 22.15 to 37.95, suggesting that $CI1$ is able to detect small increases in cyanobacteria concentration. However, in the absence of cyanobacteria, it is higher than 0, which suggests an offset problem. This erroneous offset may be explained by the need for accurate local parameterization [52].

The second index, $CI2$, uses the band ratio between water reflectance at 600 nm and 700 nm [15]. Figure 11 confirms the interest of the 600 nm spectral band as the second derivative is positive in the presence of cyanobacteria and negative otherwise. In fact, a positive second derivative means that the curve is convex, which is consistent with the PC

pigment absorption. As for $CI1$, one can notice that $CI1$ increases with the concentration of cyanobacteria.

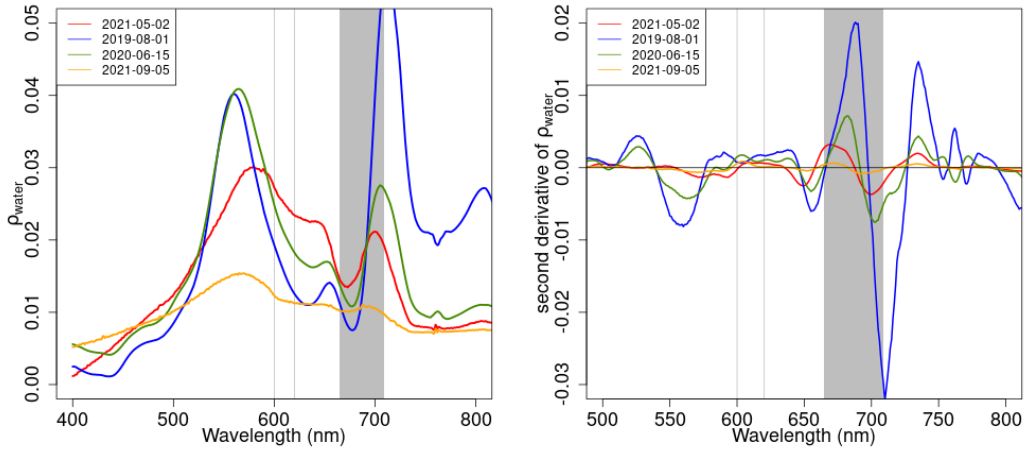

Figure 11. Average reflectance spectra for a diatom bloom (2021-05-02) and from cyanobacteria blooms (2019-08-01, 2020-06-15 and 2021-09-05) (**left**) and second derivatives for each spectra (**right**). Gray vertical lines at 600 and 620 nm and shaded areas between 665 and 709 nm show the wavelengths of interest.

The third index, $CI3$, is expected to have a negative value in the presence of cyanobacteria and a positive value otherwise [48]. Our results show that $CI3$ is not able to detect cyanobacteria blooms with a concentration of 4.7 mgm^{-3}, as $CI3$ is null in these cases, whereas it is slightly negative when no cyanobacteria are observed. However, for higher concentrations of cyanobacteria, $CI3$ is significantly lower, suggesting that this index can only be used to detect important changes in cyanobacteria concentrations. As the spectral region (i.e., 665–709 nm) is also highly impacted by Chl_a absorption, it is possible that variability in Chl_a concentration also affects $CI3$.

Table 3. Phytoplankton parameters measured in the Blankaart reservoir at the same date as water reflectance spectra displayed in Figure 9 and cyanobacteria indexes (CI) calculated from the water reflectance. See text for details about the different CI.

Date	Sensor	Diatoms (µg/L)	Cyano (µg/L)	Chl_a µg/L)	$CI1$	$CI2$	$CI3$
2019-08-01	PANTHYR	0	41.58	328.6	426.41	2.073	−0.020
2020-06-15	PANTHYR	0	11.80	32.5	82.57	1.046	−0.007
2021-05-02	HYPSTAR	29.18	0	39.4	22.15	0.777	−0.001
2021-09-05	HYPSTAR	0	4.7	24.2	37.95	0.86	0.00

4. Discussion

4.1. Further Improving HYPSTAR Derived Water Quality Products

The results above confirm that the HYPSTAR system provides valuable data at very high temporal resolution with low manpower requirements. Currently, the data are processed automatically and shared with the water managers for monitoring trends of Chl_a in the water reservoir and to investigate the effectiveness of the strategies to control algal blooms. Hence, the HYPSTAR can be used as a quick and cost-effective method to monitor water quality and detect algal blooms, provided that an initial phase of quality check is performed followed by a tuning and validation of the water quality algorithms. However, further improvement in the data processing may aid in reducing the inaccuracies in water quality products, and increase the number of data. For instance, improving the correction for the air–water interface reflectance will reduce the number of spectra removed by the

quality checks (e.g., negative reflectance). The present study relies on external wind speed reflectance data to correct the upwelling radiance for air–water interface reflectance and retrieves the air–water interface reflectance factor, ρ_F in Equation (1), based on the look-up tables of [26]. However, radiative transfer simulations were made by [26] with simulated sea surfaces, where the wave slope statistics match those of the Cox–Munk model [53] based on an input wind speed. These wave models assume a fully developed wind wave sea, where the wave field is in equilibrium with the local wind. This assumption is often not valid, especially for fetch-limited conditions typical of inland waters. In addition, the 400 m long wall within the reservoir significantly affects the wind at the water surface. Hence, the VLINDER wind speed may differ from the wind speed that should be considered to obtain the proper wave slope statistics at the surface. To increase the accuracy of the reflectance data, the HYPSTAR should be placed further away from the wall (i.e., increase the distance between the wall and the field-of-view of the sensor), and the processing could be improved by testing other methods to correct for the air–water interface reflectance (e.g., see [6] and references therein).

The results show that the retrieved Chl_a concentrations closely follow the water sampling data. However, more coincident HYPSTAR and water sampling data are required to further validate the algorithms and cover a larger range of Chl_a concentrations. Indeed most values for the validation of the algorithms are below 15µg/L, which is not considered to be harmful for the drinking water production. In addition, as mentioned earlier, the CRAT algorithm with λ_2 retrieved in the 704–740 nm spectral range is not expect to perform well outside the ∼12–120 µg/L. Hence, a proper validation of the CRAT algorithm requires additional data in this concentration range. For higher concentrations of Chl_a (i.e., >100 µg/L), we could also test the same algorithm but using λ_2 >= 825 nm, as suggested by Ruddick et al. [34].

The rapid testing of different cyanobacteria indexes confirms that the data from autonomous hyperspectral radiometers have the potential to monitor the real-time presence/absence of cyanobacteria. However, a larger dataset of coincident water sampling and radiometric data is required to further validate these algorithms and possibly quantify the cyanobacteria biomass. Indeed, in our dataset only very moderated cyanobacteria blooms were recorded during the HYPSTAR deployment, while strong cyanobacteria bloom events were recorded during the PANTHYR deployment. However, the number of valid matchups between in situ samples and radiometric data was low (i.e., 4). The results only allow us to analyze certain spectra and test some algorithms without being able to provide a proper calibration. Nevertheless, the results tend to confirm the feasibility of monitoring cyanobacteria bloom with both HYPSTAR and PANTHYR. Since water sampling and HYPSTAR are still ongoing, the number of match-ups is expected to increase and new algorithms may be developed in the future using the very high spectral resolution of the HYPSTAR. Indeed, by focusing on very small regions of the spectra, we could limit the impact of non-specific pigments (e.g., using the spectral position of the second-derivative minimum or maximum [54]).

4.2. Early Warnings and Spatial Monitoring

With its very high temporal resolution, the autonomous hyperspectral radiometers may be used to obtain first warnings and, when required, to take actions before bloom. In addition to the water quality products mentioned here, i.e., Chl_a and SPM, radiance and irradiance data may therefore also be used to approximate environmental conditions known to influence the development of algal blooms. For instance, downwelling irradiance measurements can be used as a proxy for air temperature and sun illumination. Upwelling radiance measurements taken within the principal plane may also be used to estimate the wind speed at the air–water surface [55], and, subsequently, serve to investigate the degree of water column stratification.

While the HYPSTAR depicts very small water quality variations over time, it is limited by the first optical depth and does not provide a synoptic view of the entire reservoir. Therefore, Chl_a concentrations may be underestimated when blooms occur deeper in the water column, and complementary online in-water monitoring systems may be useful. Monitoring the spatial variability of the water quality products is also essential for effective water management, e.g., to ensure the better efficiency of strategies and control algal growth by acting over given sites within the reservoir. The Landsat-9 and Sentinel-2B images shown in Figure 10 confirm this need by showing how significantly the water properties may vary spatially over the reservoir. To exploit satellite images over the reservoir, common atmospheric correction algorithms for high spatial resolution images, such as ACOLITE [23], need to be improved. Indeed, due to the relatively small extent of the water reservoir, the satellite also records the light that has been reflected or emitted from adjacent vegetation pixels and scattered by the atmosphere within the field of view of the sensor [56]. Hence, atmospheric correction should also correct for the adjacency effect. The HYPSTAR measurements therefore represent very valuable validation data.

5. Conclusions

This study shows the feasibility of using hyperspectral remote sensing techniques as a rapid assessment tool for monitoring water quality. The results illustrate the benefits of hyperspectral data with very high temporal resolution. Compared with the water sampling points, the autonomous measurements were able to depict small temporal variations in Chl_a concentrations and SPM over long periods of time and required very limited manpower. Hyperspectral sensors also aid in retrieving more advanced water quality parameters relying on very fine spectral features (e.g., for the detection of cyanobacteria). The HYPSTAR data should be further complemented with satellite images to provide a synoptic view of the reservoir, both spatially and temporally. Meanwhile, these data will also be valuable to validate the performance of the atmospheric correction algorithms over inland waters (in particular, the algorithms for the correction of adjacency effects). While timely and accurate water quality estimates are required to catch the heterogeneous and ephemeral nature of algae blooms, our results show that hyperspectral remote sensing sensors such as HYPSTAR may be confidently used to obtain first warnings and, when required, to take actions before bloom—ultimately, helping the management of drinking and recreational reservoirs with prime water quality data.

Author Contributions: Conceptualization, C.G. and H.L.; methodology and software, C.G., H.L. and A.D.; investigation, C.G., H.L., A.D. and H.V.; validation, C.G., H.L. and A.D.; writing—original draft preparation, C.G., H.L. and A.D.; writing—review and editing, C.G., H.L., A.D. and H.V.; project administration, C.G. and H.V.; funding acquisition, C.G. and H.V. All authors have read and agreed to the published version of the manuscript.

Funding: HYPSTAR deployment and maintenance and raw HYPSTAR data storage and processing were funded by the H2020 Project HYPERNETS (grant number: 775983). The analysis and quality check of the reflectance data, the validation of the water quality products, and the processing of the satellite data were funded by the BELSPO STEREO III Project GLAD4ADRINK (grant number: SR/36/343). The improvement and validation of advanced water quality products was funded by the H2020 Project CALLISTO (grant number: 101004152).

Data Availability Statement: HYPSTAR data are currently accessible for the site operators and managers and will become publicly available with the license Attribution NonCommercial NoDerivs, CC BY-NC-ND, through WATERHYPERNET (https://waterhypernet.org/, accessed on 14 October 2022) after the H2020 HYPERNETS project (May 2023).

Acknowledgments: The authors would like to thank Quinten Vanhellemont for his support with ACOLITE and his help with the processing of the satellite images, and Ingrid Keupers for her relevant comments and suggestions on our data analysis and results. The University of Ghent, PIs, and the maintenance staff of the VLINDER weather stations are greatly acknowledged for

distributing the VLINDER data. The anonymous reviewers are also acknowledged for their comments and suggestions.

Conflicts of Interest: The authors declare no conflicts of interest.

References

1. European Environment Agency. *Water Resources across Europe: Confronting Water Stress: An Updated Assessment*; Publications Office: Luxembourg, 2021.
2. Schaeffer, B.A.; Schaeffer, K.G.; Keith, D.; Lunetta, R.S.; Conmy, R.; Gould, R.W. Barriers to adopting satellite remote sensing for water quality management. *Int. J. Remote Sens.* **2013**, *34*, 7534–7544. [CrossRef]
3. Moore, C.; Barnard, A.; Fietzek, P.; Lewis, M.R.; Sosik, H.M.; White, S.; Zielinski, O. Optical tools for ocean monitoring and research. *Ocean Sci.* **2009**, *5*, 661–684. [CrossRef]
4. Storey, M.V.; van der Gaag, B.; Burns, B.P. Advances in on-line drinking water quality monitoring and early warning systems. *Water Res.* **2011**, *45*, 741–747. [CrossRef]
5. IOCCG. *Synergy between Ocean Colour and Biogeochemical—Ecosystem Models*; Reports of the International Ocean-Colour Coordinating Group; Dutkiewicz, S., Ed.; IOCCG: Dartmouth, NS, Canada, 2020; Volume 19. [CrossRef]
6. Ruddick, K.; Voss, K.; Boss, E.; Castagna, A.; Frouin, R.; Gilerson, A.; Hieronymi, M.; Johnson, B.C.; Kuusk, J.; Lee, Z.; et al. A Review of Protocols for Fiducial Reference Measurements of WaterLeaving Radiance for Validation of Satellite Remote-Sensing Data over Water. *Remote Sens.* **2019**, *11*, 2198. [CrossRef]
7. Vandermeulen, R.A.; Mannino, A.; Neeley, A.; Werdell, J.; Arnone, R. Determining the optimal spectral sampling frequency and uncertainty thresholds for hyperspectral remote sensing of ocean color. *Opt. Express* **2017**, *25*, A785. [CrossRef]
8. Wolanin, A.; Soppa, M.; Bracher, A. Investigation of Spectral Band Requirements for Improving Retrievals of Phytoplankton Functional Types. *Remote Sens.* **2016**, *8*, 871. [CrossRef]
9. Chang, G.; Mahoney, K.; Briggs-Whitmire, A.; Kohler, D.; Mobley, C.; Lewis, M.; Moline, M.; Boss, E.; Kim, M.; Philpot, W.; et al. The New Age of Hyperspectral Oceanography. *Oceanography* **2004**, *17*, 16–23. [CrossRef]
10. Soja-Woźniak, M.; Darecki, M.; Wojtasiewicz, B.; Bradtke, K. Laboratory measurements of remote sensing reflectance of selected phytoplankton species from the Baltic Sea. *Oceanologia* **2018**, *60*, 86–96. [CrossRef]
11. Dierssen, H.; Bracher, A.; Brando, V.; Loisel, H., Ruddick, K. Data Needs for Hyperspectral Detection of Algal Diversity Across the Globe. *Oceanography* **2020**, *33*, 74–79. [CrossRef]
12. Palmer, S.C.; Kutser, T.; Hunter, P.D. Remote sensing of inland waters: Challenges, progress and future directions. *Remote Sens. Environ.* **2015**, *157*, 1–8. [CrossRef]
13. Randolph, K.; Wilson, J.; Tedesco, L.; Li, L.; Pascual, D.L.; Soyeux, E. Hyperspectral remote sensing of cyanobacteria in turbid productive water using optically active pigments, Chlorophyll-*a* and phycocyanin. *Remote Sens. Environ.* **2008**, *112*, 4009–4019. [CrossRef]
14. Simis, S.G.H.; Peters, S.W.M.; Gons, H.J. Remote sensing of the cyanobacterial pigment phycocyanin in turbid inland water. *Limnol. Oceanogr.* **2005**, *50*, 237–245. [CrossRef]
15. Mishra, S.; Mishra, D.; Schluchter, W. A Novel Algorithm for Predicting Phycocyanin Concentrations in Cyanobacteria: A Proximal Hyperspectral Remote Sensing Approach. *Remote Sens.* **2009**, *1*, 758–775. [CrossRef]
16. Vansteenwegen, D.; Ruddick, K.; Cattrijsse, A.; Vanhellemont, Q.; Beck, M. The Pan-and-Tilt Hyperspectral Radiometer System (PANTHYR) for Autonomous Satellite Validation Measurements—Prototype Design and Testing. *Remote Sens.* **2019**, *11*, 1360. [CrossRef]
17. Zibordi, G.; Mélin, F.; Berthon, J.F.; Holben, B.; Slutsker, I.; Giles, D.; D'Alimonte, D.; Vandemark, D.; Feng, H.; Schuster, G.; et al. AERONET-OC: A Network for the Validation of Ocean Color Primary Products. *J. Atmos. Ocean. Technol.* **2009**, *26*, 1634–1651. [CrossRef]
18. Wang, Z.; Costa, M. Autonomous Shipborne In Situ Reflectance Data in Optically Complex Coastal Waters: A Case Study of the Salish Sea, Canada *Front. Remote Sens.* **2022**, *3*, 867570. [CrossRef]
19. Cullen, J.J.; Ciotti, A.M.; Davis, R.F.; Lewis, M.R. Optical detection and assessment of algal blooms. *Limnol. Oceanogr.* **1997**, *42*, 1223–1239. [CrossRef]
20. Muller-Karger, F.E.; Hestir, E.; Ade, C.; Turpie, K.; Roberts, D.A.; Siegel, D.; Miller, R.J.; Humm, D.; Izenberg, N.; Keller, M.; et al. Satellite sensor requirements for monitoring essential biodiversity variables of coastal ecosystems. *Ecol. Appl.* **2018**, *28*, 749–760. [CrossRef]
21. Song, K.; Li, L.; Tedesco, L.; Clercin, N.; Hall, B.; Li, S.; Shi, K.; Liu, D.; Sun, Y. Remote estimation of phycocyanin (PC) for inland waters coupled with YSI PC fluorescence probe. *Environ. Sci. Pollut. Res.* **2013**, *20*, 5330–5340. [CrossRef]
22. Goyens, C.; De Vis, P.; Hunt, S.E. Automated Generation of Hyperspectral Fiducial Reference Measurements of Water and Land Surface Reflectance for the Hypernets Networks. In Proceedings of the 2021 IEEE International Geoscience and Remote Sensing Symposium IGARSS, Brussels, Belgium, 11–16 July 2021; pp. 7920–7923. [CrossRef]
23. Vanhellemont, Q. Adaptation of the dark spectrum fitting atmospheric correction for aquatic applications of the Landsat and Sentinel-2 archives. *Remote Sens. Environ.* **2019**, *225*, 175–192. [CrossRef]
24. Mueller, J.L.; Morel, A.; Frouin, R.; Davis, C.; Arnone, R.; Carder, K.; Lee, Z.P.; Steward, R.G.; Hooker, S.; Mobley, C.D.; et al. *Ocean Optics Protocols for Satellite Ocean Color Sensor Validation, Revision 4, Volume III: Radiometric Measurements and Data Analysis Protocols*; Goddard Space Flight Space Center: Greenbelt, MD, USA, 2003.

25. IOCCG. Ocean Optics and Biogeochemistry Protocols for Satellite Ocean Colour Sensor Validation, Volume 3.0: Protocols for Satellite Ocean Colour Data Validation: In Situ Optical Radiometry. In *IOCCG Ocean Optics and Biogeochemistry Protocols for Satellite Ocean Colour Sensor Validation*; Zibordi, G., Voss, K., Johnson, B.C., Meuller, J.L., Eds.; International Ocean Colour Coordinating Group (IOCCG): Dartmouth, NS, Canada, 2019; Volume 3, 67p. [CrossRef]
26. Mobley, C.D. Estimation of the remote-sensing reflectance from above-surface measurements. *Appl. Opt.* **1999**, *38*, 7442. [CrossRef] [PubMed]
27. Caluwaerts, S.; Top, S.; Vergauwen, T.; Wauters, G., De Ridder, K.; Hamdi, R.; Mesuere, B.; Van Schaeybroeck, B.; Wouters, H.; Termonia, P. Engaging schools to explore meteorological observational gaps. *Bull. Am. Meteorol. Soc.* **2021**, 1–17. [CrossRef]
28. Ruddick, K.; De Cauwer, V.; Van Mol, B. Use of the near infrared similarity reflectance spectrum for the quality control of remote sensing data. In *Remote Sensing of the Coastal Oceanic Environment*; Frouin, R.J., Babin, M., Sathyendranath, S., Eds.; SPIE: Bellingham, WA, USA, 2005; p. 588501. [CrossRef]
29. Groetsch, P.M.M.; Gege, P.; Eleveld, M.A.; Peters, S.W.M. Validation of a spectral correction procedure for sun and sky reflections in above-water reflectance measurements. *Opt. Express* **2017**, *25*, A742–A761. [CrossRef] [PubMed]
30. Ruddick, K.G.; Cauwer, V.D.; Park, Y.J.; Moore, G. Seaborne measurements of near infrared water-leaving reflectance: The similarity spectrum for turbid waters. *Limnol. Oceanogr.* **2006**, *51*, 13. [CrossRef]
31. Bridgewater, L.L.; Baird, R.B.; Eaton, A.D.; Rice, E.W.; Association, A.P.H.; Association, A.W.W.; Federation, W.E. (Eds.) *Standard Methods for the Examination of Water and Wastewater*, 23rd ed.; American Public Health Association: Washington, DC, USA, 2017.
32. EMIS; VITO. Compendium voor de Monsterneming, Meting en Analyse van Water (WAC). 2020. Available online: https://emis.vito.be/nl/erkende-laboratoria/water-gop/compendium-wac (accessed on 14 October 2022).
33. CEN. *EN 15204*; Water Quality—Guidance Standard on the Enumeration of Phytoplankton Using Inverted Microscopy (Utermöhl Technique). European Committee for Standardization: Brussels, Belgium, 2006. Available online: https://www.en-standard.eu/bs-en-15204-2006-water-quality-guidance-standard-on-the-enumeration-of-phytoplankton-using-inverted-microscopy-utermoehl-technique/ (accessed on 14 October 2022).
34. Ruddick, K.G.; Gons, H.J.; Rijkeboer, M.; Tilstone, G. Optical remote sensing of Chlorophyll-*a* in case 2 waters by use of an adaptive two-band algorithm with optimal error properties. *Appl. Opt.* **2001**, *40*, 3575. [CrossRef]
35. Lavigne, H.; Van der Zande, D.; Ruddick, K.; Cardoso Dos Santos, J.; Gohin, F.; Brotas, V.; Kratzer, S. Quality-control tests for OC4, OC5 and NIR-red satellite Chlorophyll-*a* algorithms applied to coastal waters. *Remote Sens. Environ.* **2021**, *255*, 112237. [CrossRef]
36. Lee, Z.; Carder, K.L.; Arnone, R.A. Deriving inherent optical properties from water color: A multiband quasi-analytical algorithm for optically deep waters. *Appl. Opt.* **2002**, *41*, 5755–5772. [CrossRef]
37. Werdell, P.J.; Franz, B.A.; Bailey, S.W.; Feldman, G.C.; Boss, E.; Brando, V.E.; Dowell, M.; Hirata, T.; Lavender, S.J.; Lee, Z.; et al. Generalized ocean color inversion model for retrieving marine inherent optical properties. *Appl. Opt.* **2013**, *52*, 2019–2037. [CrossRef]
38. Gons, H.J. Optical Teledetection of Chlorophyll *A* Turbid Inland Waters. *Environ. Sci. Technol.* **1999**, *33*, 1127–1132. [CrossRef]
39. Gons, H.J.; Auer, M.T.; Effler, S.W. MERIS satellite chlorophyll mapping of oligotrophic and eutrophic waters in the Laurentian Great Lakes. *Remote Sens. Environ.* **2008**, *112*, 4098–4106. [CrossRef]
40. Buiteveld, H.; Hakvoort, J.H.M.; Donze, M. Optical properties of pure water. In *Ocean Optics XII*; Jaffe, J.S., Ed.; SPIE: Bellingham, WA, USA, 1994; pp. 174–183. [CrossRef]
41. Bricaud, A.; Babin, M.; Morel, A.; Claustre, H. Variability in the chlorophyll-specific absorption coefficients of natural phytoplankton: Analysis and parameterization. *J. Geophys. Res.* **1995**, *100*, 13321. [CrossRef]
42. Bramich, J.; Bolch, C.J.; Fischer, A. Improved red-edge Chlorophyll-*a* detection for Sentinel 2. *Ecol. Indic.* **2021**, *120*, 106876. [CrossRef]
43. Gilerson, A.A.; Gitelson, A.A.; Zhou, J.; Gurlin, D.; Moses, W.; Ioannou, I.; Ahmed, S.A. Algorithms for remote estimation of Chlorophyll-*a* in coastal and inland waters using red and near infrared bands. *Opt. Express* **2010**, *18*, 24109. [CrossRef]
44. Paavel, B.; Kangro, K.; Arst, H.; Reinart, A.; Kutser, T.; Nõges, T. Parameterization of chlorophyll-specific phytoplankton absorption coefficients for productive lake waters. *J. Limnol.* **2016**, *75*, 423–438. [CrossRef]
45. Nechad, B.; Ruddick, K.; Park, Y. Calibration and validation of a generic multisensor algorithm for mapping of total suspended matter in turbid waters. *Remote Sens. Environ.* **2010**, *114*, 854–866. [CrossRef]
46. Dogliotti, A.; Ruddick, K.; Nechad, B.; Doxaran, D.; Knaeps, E. A single algorithm to retrieve turbidity from remotely-sensed data in all coastal and estuarine waters. *Remote Sens. Environ.* **2015**, *156*, 157–168. [CrossRef]
47. Warren, M.A.; Simis, S.G.; Selmes, N. Complementary water quality observations from high and medium resolution Sentinel sensors by aligning Chlorophyll-*a* and turbidity algorithms. *Remote Sens. Environ.* **2021**, *265*, 112651. [CrossRef]
48. Wynne, T.T.; Stumpf, R.P.; Tomlinson, M.C.; Dyble, J. Characterizing a cyanobacterial bloom in Western Lake Erie using satellite imagery and meteorological data. *Limnol. Oceanogr.* **2010**, *55*, 2025–2036. [CrossRef]
49. Spyrakos, E.; O'Donnell, R.; Hunter, P.D.; Miller, C.; Scott, M.; Simis, S.G.H.; Neil, C.; Barbosa, C.C.F.; Binding, C.E.; Bradt, S.; et al. Optical types of inland and coastal waters: Optical types of inland and coastal waters. *Limnol. Oceanogr.* **2018**, *63*, 846–870. [CrossRef]
50. Gitelson, A.A.; Merzlyak, M.N.; Lichtenthaler, H.K. Detection of Red Edge Position and Chlorophyll Content by Reflectance Measurements Near 700 nm. *J. Plant Physiol.* **1996**, *148*, 501–508. [CrossRef]
51. Kudela, R.M.; Palacios, S.L.; Austerberry, D.C.; Accorsi, E.K.; Guild, L.S.; Torres-Perez, J. Application of hyperspectral remote sensing to cyanobacterial blooms in inland waters. *Remote Sens. Environ.* **2015**, *167*, 196–205. [CrossRef]

52. Duan, H.; Ma, R.; Hu, C. Evaluation of remote sensing algorithms for cyanobacterial pigment retrievals during spring bloom formation in several lakes of East China. *Remote Sens. Environ.* **2012**, *126*, 126–135. [CrossRef]
53. Cox, C.; Munk, W. Measurement of the Roughness of the Sea Surface from Photographs of the Sun's Glitter. *J. Opt. Soc. Am.* **1954**, *44*, 838. [CrossRef]
54. Lubac, B.; Loisel, H.; Guiselin, N.; Astoreca, R.; Felipe Artigas, L.; Mériaux, X. Hyperspectral and multispectral ocean color inversions to detect *Phaeocystis Globosa* Bloom. Coast. Waters. *J. Geophys. Res.* **2008**, *113*, C06026. [CrossRef]
55. Goyens, C.; Ruddick, K. Improving the standard protocol for above-water reflectance measurements: 1. Estimating effective wind speed from angular variation of sunglint. *Appl. Opt.* 2022, *submitted*.
56. Pahlevan, N.; Mangin, A.; Balasubramanian, S.V.; Smith, B.; Alikas, K.; Arai, K.; Barbosa, C.; Bélanger, S.; Binding, C.; Bresciani, M.; et al. ACIX-Aqua: A global assessment of atmospheric correction methods for Landsat-8 and Sentinel-2 over lakes, rivers, and coastal waters. *Remote Sens. Environ.* **2021**, *258*, 112366. [CrossRef]